JOURNAL OF MATERIALS SCIENCE 26 (1991) 1266–1276

Microstructure–cooling rate correlations in melt-spun alloys

B. CANTOR, W. T. KIM, B. P. BEWLAY*, A. G. GILLEN‡
Department of Materials, University of Oxford, Parks Road, Oxford OX1 3PH, UK

Photocalorimetric techniques have been used to measure top surface temperatures during melt spinning of Ni–Al and 316L stainless steel ribbons, in order to investigate the effect of cooling rate on the melt-spun alloy microstructures. Cooling conditions during melt-spinning are found to be near-Newtonian, with mean cooling rates, heat transfer coefficients and Nusselt numbers in the range 4×10^4 to 5×10^5 K sec^{-1}, 5×10^4 to 3×10^5 W m^{-2} K^{-1} and 0.07 to 0.22, respectively, for wheel speeds in the range 4 to 36 m sec^{-1}. The cooling rate during melt-spinning is directly proportional to the wheel speed and inversely proportional to the square of the ribbon thickness. Melt-spun Ni–Al and 316L stainless steel ribbons exhibit a columnar through-thickness solidification microstructure, with a segregation-free region adjacent to the wheel surface. Solidification takes place by heterogeneous nucleation of the undercooled liquid on the wheel surface, followed by partitionless solidification during recalescence, and finally cellular breakdown and segregated solidification. The columnar grain size decreases and the fractional segregation-free thickness increases with increasing wheel speed and cooling rate, indicating that the nucleation undercooling in the liquid is proportional to the cooling rate.

1. Introduction

Compared with conventional solidification methods, rapid solidification techniques produce microstructures with refined grain sizes, increased solubility of alloying elements and impurities, reduced levels of segregation, and in some cases the formation of metastable crystalline and amorphous phases [1–4]. In many alloy systems, these effects lead to beneficial improvements in mechanical, magnetic, electrical and other properties. Rapid solidification processing is therefore being used increasingly to manufacture metallurgical materials which take advantage of these improved properties in a variety of applications [1–4].

In all rapid solidification techniques, a mass of liquid metal or alloy is manipulated so as to be thin in at least one dimension, and at the same time in good thermal contact with an efficient heat sink. Under these conditions, heat is extracted quickly from the liquid mass, which then cools and solidifies rapidly. Typical liquid thicknesses are in the range 10 to 100 μm with corresponding cooling rates of 10^5 to 10^6 K sec^{-1}, so that cooling and solidification is complete within a few milliseconds [5–8]. Temperatures must be recorded in a very short time interval in order to measure the cooling rate during rapid solidification, and for this reason relatively few direct measurements of cooling rate have been reported [5–8]. Indirect estimates of cooling rate have been obtained from the scale of microstructural features such as grain size, dendrite arm spacing, eutectic interphase spacing and dislocation density. However, these indirect estimates are somewhat higher than expected from direct measurements, and may in any case be unreliable since microstructure-cooling rate correlations established at low cooling rates must be assumed to remain valid at high cooling rates [5–8].

In order to maximize the advantages of manufacturing alloys by rapid solidification processing, it is clearly essential to control the cooling rate so as to obtain a reproducible microstructure. The aim of the present paper is to discuss the relationship between cooling rate and microstructure in melt-spun Ni–Al alloys and 316L stainless steel. Cooling rates have been measured by photocalorimetry, and microstructures have been examined by optical metallography. The variation of microstructure as a function of cooling rate gives some insight into the mechanism by which solidification takes place during melt-spinning.

2. Experimental procedure

Binary Ni–Al alloys were manufactured from 99.99% pure nickel and 99.999% pure aluminium which were cleaned, weighed, put into recrystallized alumina crucibles, and r.f. induction-melted in a vacuum chamber back-filled with argon at 53 kPa. When each alloy charge was molten, there was a further period of

---

* *Present address*: GE Corporate Research & Development, PO Box 8, Schenectady, NY 12301, USA.
‡ *Present address*: Department of Materials Engineering, Drexel University, Philadelphia, PA 19104, USA.

heating lasting at least 15 min to ensure good mixing of the melt, followed by casting under the argon atmosphere in the vacuum chamber into a split graphite mould to produce lengths of 6.5 mm diameter rod suitable for the melt-spinning apparatus. Melt-spinning experiments were performed on alloys containing 5 and 11 wt % Al, with liquidus temperatures of 1440 and 1388 °C, and solidus temperatures of 1430 and 1379 °C, respectively [9]. Melt-spinning experiments were also performed on a commercial 316L stainless steel, supplied in the form of bar stock, with a chemically analysed composition of Fe–17.44 wt % Cr–10.90 wt % Ni–2.36 wt % Mo–1.03 wt % Si–0.64 wt % Mn–0.026 wt % C–0.011 wt % S–0.005 wt % N–0.003 wt % P. A Dupont 1090 thermal analyser was used to determine the liquidus and solidus temperatures of the commercial 316L stainless steel as 1463 and 1443 °C, respectively [10].

For melt-spinning, individual specimens of approximately 10 g were placed in a quartz nozzle of 7 mm internal diameter with a circular orifice of 1 mm diameter, r.f. induction melted under argon, and then ejected by an argon gas overpressure on to the 1200C SiC abraded outer surface of a 150 mm diameter rotating copper wheel. During each melt-spinning run, the wheel speed was measured with a Compact 6000 tachometer, the argon gas ejection overpressure with an in-line pressure gauge, and the melt temperature with a Land Cyclops 51 optical pyrometer. The pyrometer was calibrated for each alloy in a separate series of experiments against a Pt/Pt–13% Rh thermocouple inside a cylindrical alloy charge, which was r.f. induction heated in a quartz nozzle under identical conditions to those used during melt spinning. The Ni–Al alloy melt-spinning runs were performed with an argon overpressure in the range 21 to 42 kPa, a melt superheat in the range 170 to 230 °C, and a wheel speed in the range 12 to 36 m sec^{-1}. The 316L stainless steel melt-spinning runs were performed with an argon overpressure of 14 kPa, a melt superheat of 90 °C, and a wheel speed in the range 4 to 32 m sec^{-1}. During melt-spinning of 316L stainless steel, the entire melt-spinning apparatus was enclosed in a glass bell jar which was evacuated to 10 Pa and then backfilled with argon at 48 kPa so as to prevent oxidation of the steel after ejection from the quartz nozzle. This was not necessary during melt-spinning of the Ni–Al alloys, which showed no evidence of oxidation without the bell jar.

The melt-spinning conditions described above produced melt-spun ribbons which were typically several metres long, 2 to 5 mm wide and 20 to 120 μm thick, and which were suitable both for cooling rate measurements during melt-spinning and for subsequent microstructural examination using optical microscopy. Ribbon microstructures were examined in an Olympus BH optical microscope on longitudinal, through-thickness sections which were mounted in resin, ground and polished to 0.25 μm diamond, and then etched in 5% hydrogen peroxide–40% hydrochloric acid–55% water for the Ni–Al alloys, and 10% oxalic acid–90% water for the 316L stainless steel. Ribbon thicknesses and the scale of microstructural features were measured with an eyepiece graticule in the optical microscope.

Cooling rates were measured by a photocalorimetric technique [10–13]. During each melt-spinning run, the top surface of the ribbon was photographed with an Olympus OM-2N camera, using Ektachrome 200ASA daylight transparency film, exposed by a cable release and motor drive at a frame rate of 2 or 5 sec^{-1}, with an exposure time of 1 msec and an aperture of f22. A Vivitar zoom lens set at 70 mm and extension tubes with a total length of 68 mm enabled the camera to be positioned 100 mm from the quartz nozzle and still produce close-up macro-images of the Ni–Al ribbon top surfaces during melt-spinning. Similar images of the 316L stainless steel ribbon top surfaces were obtained with a zoom lens setting of 105 mm, extension tube length of 56 mm, and the camera positioned 130 mm from the quartz nozzle, just outside the glass bell jar. To enable subsequent calibration of the film colour density against temperature, ribbons of each alloy were later reheated using a direct electric current, to give a range of temperatures which were measured either by the Land pyrometer or by 130 μm diameter Pt/Pt–13% Rh thermocouple wires spot-welded to the ribbon surface. The Olympus camera was again used to photograph the reheated ribbons at each temperature. During reheating of the ribbons, the camera settings, film type, exposure conditions, and relative positions of ribbon, camera and pyrometer were exactly the same as those used during melt-spinning.

Photographs of each Ni–Al and 316L stainless steel ribbon during melt-spinning and reheating were developed by an E6 film process. Film colour density was subsequently quantified with a Macbeth colour transmission densitomer, which measured the intensity of red light transmitted through a 1 mm diameter aperture placed over the colour transparency film. Transparencies of the reheated ribbons were used to construct a calibration plot of film colour density against temperature for each alloy, and the densitometer was then used with the melt-spinning transparencies to measure colour density and therefore temperature at the melt puddle and at various positions along the length of each melt-spun ribbon. Distances on the melt-spinning transparencies were measured with the aid of crosswires on the densitometer and perforations on the film edge, and were converted first to true ribbon–wheel contact distances by photographing a calibration scale fixed to the copper wheel surface, and then to ribbon–wheel contact times by dividing by the wheel speed. In this way, a cooling curve of top surface ribbon temperature against ribbon–wheel contact time was obtained for each Ni–Al and 316L stainless steel melt-spun ribbon.

3. Results

Fig. 1 shows a series of typical cooling curves for Ni–5 wt % Al and 316L stainless steel ribbons, manufactured under a variety of different melt-spinning conditions. Cooling curves from ribbons melt-spun

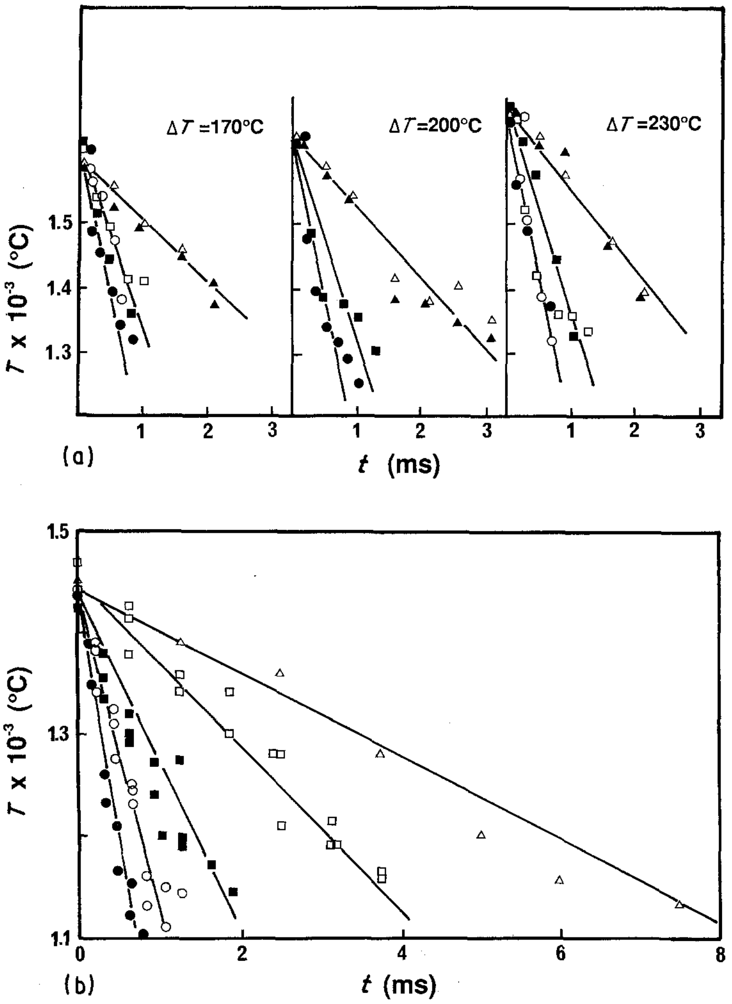

Figure 1 Photocalorimetric cooling curves showing top surface ribbon temperature as a function of time during melt-spinning, under a variety of different melt-spinning conditions. (a) Ni–5 wt % Al; values of V (m sec^{-1}) and P (kPa) as follows: (△) 12, 21; (▲) 12, 42; (□) 24, 21; (■) 24, 42; (○) 36, 21; (●) 36, 42. (b) 316L stainless steel; V (m sec^{-1}) = (△) 4, (□) 8, (■) 16, (○) 24, (●) 32 at $\Delta T = 90\,°\mathrm{C}$, $P = 14$ kPa.

under identical conditions were found to be reproducible to well within the estimated experimental error of ± 50 K and ± 0.1 msec. To a first approximation, each cooling curve showed a linear variation of top-surface ribbon temperature with ribbon–wheel contact time over the 300 to 400 K range of temperature measurements. Average cooling rates over this temperature range were therefore calculated from each cooling curve as the least-squares best-fit slope. Within the experimental error, the resulting average cooling rates were found to be independent of argon overpressure and melt superheat. Table I shows average cooling rates and average ribbon thicknesses measured at each wheel speed for Ni–Al and 316L stainless steel melt-spun ribbons. The average cooling rates were in the range 4×10^4 to 5×10^5 K sec^{-1}, and increased with increasing wheel speed and decreasing ribbon thickness as shown in Table I.

Fig. 2 shows typical optical micrographs of longitudinal through-thickness sections which were obtained from melt-spun ribbons of Ni–11 wt % Al and 316L stainless steel. Columnar grains extended through the ribbon thickness, with a segregation-free region adjacent to the bottom surface of the ribbon, and a cellular segregation pattern within the columnar grains throughout the remainder of the microstructure. The microstructures were somewhat variable along the length of each ribbon, as can be seen in Fig. 2a and b. Table II shows some measurements at each wheel speed of the columnar grain size parallel to the long ribbon dimension and close to the wheel surface, and the fractional thickness of the segregation-free region of solidification. The grain size decreased and the fractional segregation-free thickness increased with increasing wheel speed and cooling rate.

4. Discussion

4.1. Heat transfer coefficient

For perfect Newtonian cooling conditions during melt-spinning, there are no thermal gradients in either the ribbon or the wheel, and cooling of the ribbon is controlled by the rate of heat transfer across the ribbon–wheel interface. The ribbon temperature T decreases exponentially with time t [5–8, 10–14]:

$$T - T_{\mathrm{W}} = (T_{\mathrm{I}} - T_{\mathrm{W}}) \exp(-Ht/X\rho C) \qquad (1)$$

where T_{W} is the wheel temperature, T_{I} is the initial ribbon temperature (i.e. in the melt stream), H is the heat transfer coefficient at the ribbon–wheel interface, and X and ρ are the ribbon thickness and density, respectively. $C = C' + L/\Delta T_{\mathrm{S}}$ is a modified ribbon specific heat to allow approximately for evolution of latent heat during solidification, with C' the ribbon specific heat, L the latent heat, and ΔT_{S} the temperature range of solidification.

When thermal conduction in the ribbon is a significant barrier to heat removal, cooling conditions are non-Newtonian with thermal gradients through the ribbon thickness. The ribbon temperature T is then a

TABLE I Thermal conditions for melt-spun Ni–5 wt % Al and 316L stainless steel ribbons. Cooling rates are averages over the first 40 mm of ribbon formation, ribbon thicknesses are averages over the ribbon width and length, and heat transfer coefficients and Nusselt numbers are calculated by Newtonian heat flow analysis (see text)

Alloy	Wheel speed, V (m sec^{-1})	Average cooling rate, dT/dt (K sec^{-1})	Average ribbon thickness, X (μm)	Heat transfer coefficient, H (Wm^{-2}K^{-1})	Nusselt number, $Nu = HX/K$
Ni–5Al	12	9.7×10^4	74	5.6×10^4	0.07
		1.2×10^5	79	7.2×10^4	0.09
		1.2×10^5	90	1.3×10^5	0.21
	24	2.4×10^5	61	1.4×10^5	0.14
		3.1×10^5	70	1.7×10^5	0.19
		2.8×10^5	58	1.7×10^5	0.17
	36	4.6×10^5	44	1.4×10^5	0.10
		5.0×10^5	43	1.4×10^5	0.10
		4.6×10^5	43	2.1×10^5	0.15
316L	4	4.0×10^4	95	6.5×10^4	0.19
	8	7.5×10^4	67	6.3×10^4	0.12
		8.2×10^4	67	6.6×10^4	0.14
		8.7×10^4	58	6.4×10^4	0.13
	16	1.4×10^5	34	6.8×10^4	0.10
		1.3×10^5	44	7.4×10^4	0.10
		1.9×10^5	45	1.1×10^5	0.16
	24	3.0×10^5	41	1.3×10^5	0.16
		3.2×10^5	39	1.5×10^5	0.19
	32	4.3×10^5	36	1.7×10^5	0.19
		4.6×10^5	34	2.1×10^5	0.22

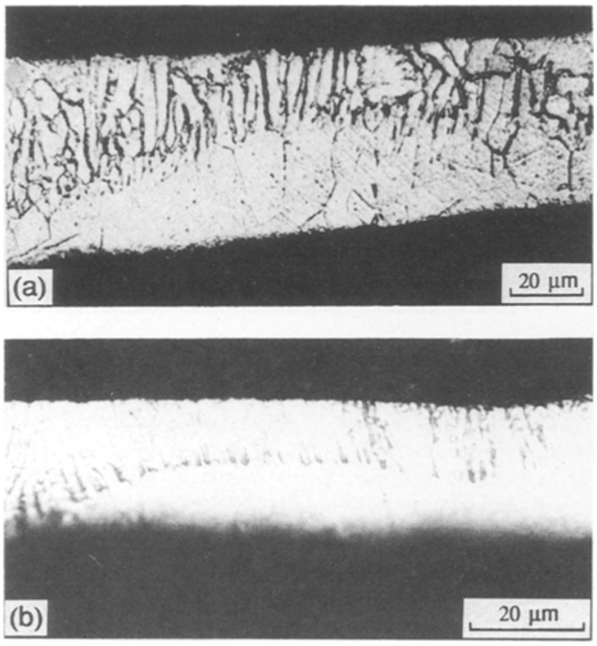

Figure 2 Longitudinal through-thickness optical micrographs of (a) Ni–11 wt % Al melt-spun at a wheel speed of 12 m sec^{-1} and (b) 316L stainless steel melt-spun at a wheel speed of 8 m sec^{-1}.

function of position x through the ribbon thickness as measured from the ribbon–wheel interface, as well as time t [5–8, 10–14]:

$$T - T_W = (T_l - T_W) \times \sum_{n=1}^{\infty} \frac{2N\cos(A_n x/X)\sec(A_n)\exp(-A_n \alpha t/X^2)}{Nu(Nu + 1) + A_n^2} \qquad (2)$$

where $Nu = HX/K$ is the Nusselt number, $\alpha = K/\rho C$ and K are the ribbon thermal diffusivity and conductivity, respectively, and the infinite series of constants A_n are the positive roots of the equation $A_n \tan A_n = Nu$. Computer calculations indicate little effect of thermal gradients in the wheel, when the wheel thermal conductivity is significantly greater than the ribbon thermal conductivity [15–17].

Fig. 3a and b show all of the cooling curves from Fig. 1a and b for melt-spun Ni–5 wt % Al and 316L stainless steel, replotted according to Equation 1; and Fig. 3c shows two of the cooling curves from Fig. 1a and b for melt-spun Ni–5 wt % Al and 316L stainless steel, replotted according to Equation 2. Heat transfer coefficients and Nusselt numbers calculated by fitting the cooling curves to Equation 1 are included in Table I for each alloy at each wheel speed. In general, cooling conditions during melt-spinning of Ni–Al alloys and 316L stainless steel are near-Newtonian, with heat transfer coefficients and Nusselt numbers in the range 5×10^4 to 3×10^5 W m^{-2} K^{-1} and 0.07 to 0.22, respectively.

4.2. Melt-spinning conditions

For near-Newtonian cooling conditions, Equation 1 reduces to a linear variation of ribbon temperature with time, when the range of measurement temperatures is relatively small and near to the melt temperature. The average cooling rate dT/dt is then given by

$$dT/dt = H(T_l - T_W)/X\rho C \qquad (3)$$

The measured cooling curves in Fig. 1 show approximately constant cooling rates for melt-spun Ni–Al alloys and 316L stainless steel, in agreement with Equation 3.

Thermal and momentum models for ribbon formation during melt-spinning indicate that the ribbon thickness varies according to a power-law relationship

TABLE II Microstructures of melt-spun Ni–5 wt % Al and 316L stainless steel ribbons. Cooling rates are averages over the first 40 mm of ribbon formation, columnar grain sizes are average measurements parallel to the long ribbon dimension and close to the wheel surface, fractional segregation-free thicknesses are maximum values observed over the ribbon width and length, and nucleation undercoolings are calculated by recalescence analysis (see text)

Alloy	Wheel speed, V (m sec^{-1})	Average cooling rate, dT/dt (K sec^{-1})	Columnar grain size, d (μm)	Fractional segregation free thickness, y/X	Nucleation undercooling, ΔT_N (K)
Ni–5Al	12	9.7×10^4	50		
		1.2×10^5	31	0.50	316
		1.2×10^5	30		
	24	2.4×10^5	18		
		3.1×10^5	26		
		2.8×10^5	30	0.66	375
	36	4.6×10^5	14		
		5.0×10^5	12		
		4.6×10^5	19		
316L	8	7.5×10^4	8		
		8.2×10^4	10	0.39	172
		8.7×10^4	12		
	16	1.4×10^5	5	0.44	191
		1.3×10^5	6		
		1.9×10^5	7		
	24	3.0×10^5	4	0.54	230
		3.2×10^5	5		

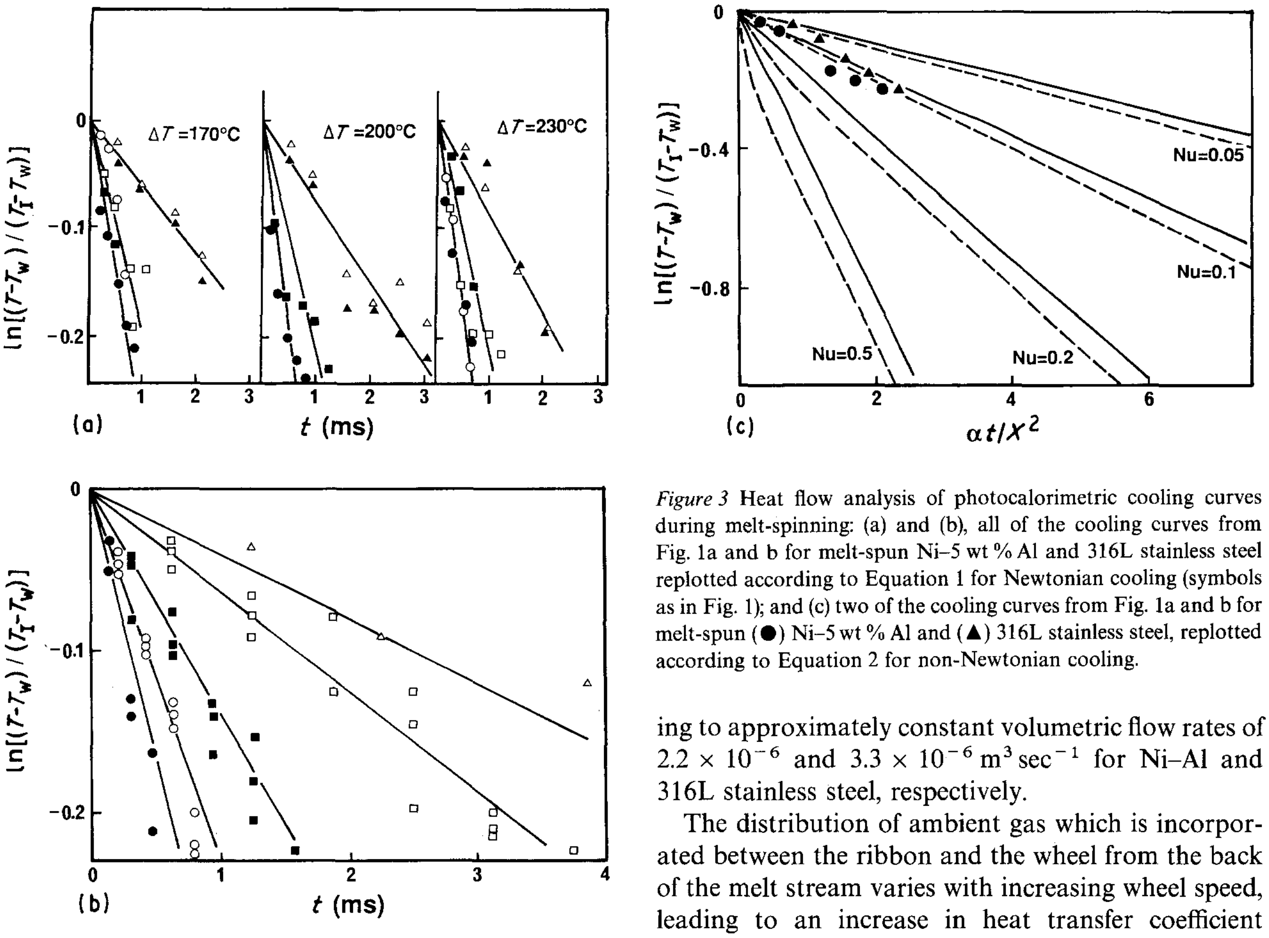

Figure 3 Heat flow analysis of photocalorimetric cooling curves during melt-spinning: (a) and (b), all of the cooling curves from Fig. 1a and b for melt-spun Ni–5 wt % Al and 316L stainless steel replotted according to Equation 1 for Newtonian cooling (symbols as in Fig. 1); and (c) two of the cooling curves from Fig. 1a and b for melt-spun (●) Ni–5 wt % Al and (▲) 316L stainless steel, replotted according to Equation 2 for non-Newtonian cooling.

with Q/V^2, where Q is the volumetric flow rate and V is the wheel speed [18, 19]. Fig. 4a and b show that the measured ribbon thicknesses against wheel speed from Table I for melt-spun Ni–Al alloys and 316L stainless steel agree with this type of power-law relationship:

$$X^2 V/Q^{1/2} = a_1 \qquad (4)$$

where a_1 is a material-dependent constant equal to 4.5×10^{-5} and 2.3×10^{-5} m$^{3/2}$ sec$^{-1/2}$, corresponding to approximately constant volumetric flow rates of 2.2×10^{-6} and 3.3×10^{-6} m^3 sec^{-1} for Ni–Al and 316L stainless steel, respectively.

The distribution of ambient gas which is incorporated between the ribbon and the wheel from the back of the melt stream varies with increasing wheel speed, leading to an increase in heat transfer coefficient [10, 12]. Fig. 5a and b show that the heat transfer coefficients in Table I for melt-spun Ni–Al alloys and 316L stainless steel fit rather approximately to a power-law relationship with wheel speed:

$$H^2/V = a_2 \qquad (5)$$

where a_2 is a constant equal to 7.8×10^8 W^2 sec m^{-5} K^{-2} for both materials.

The variation of cooling rate with wheel speed and ribbon thickness can be obtained by combining

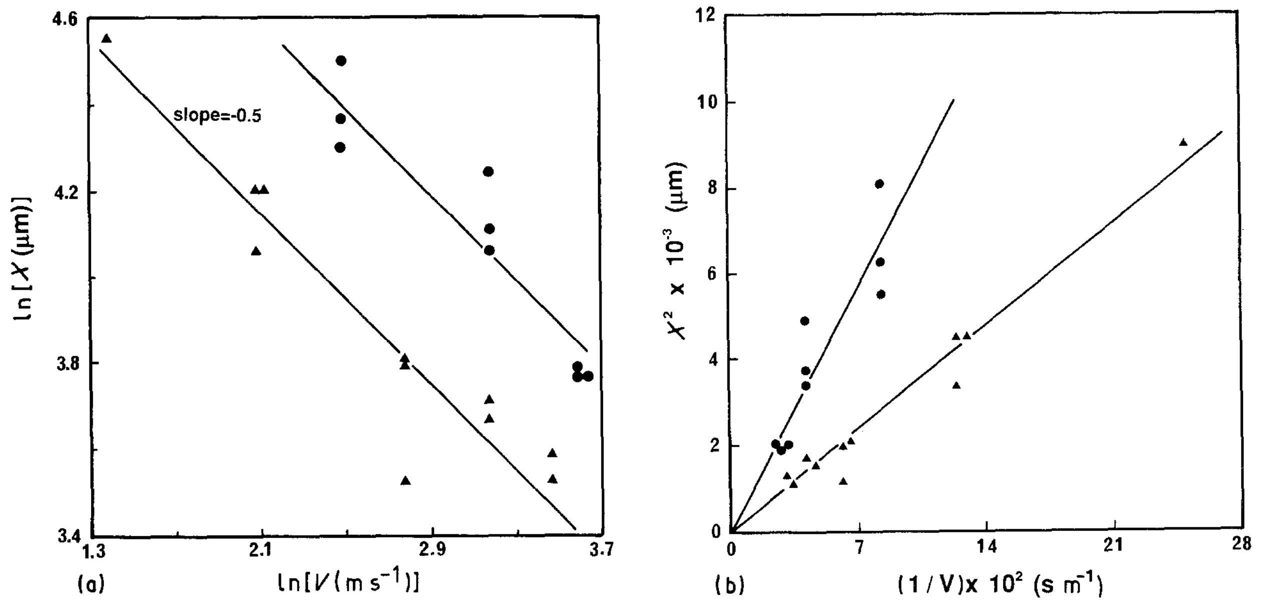

Figure 4 Variation of ribbon thickness X with wheel speed V in melt-spun (●) Ni–Al alloys and (▲) 316L stainless steel: (a) ln X against ln V with best-fit straight lines with a slope of $-1/2$; and (b) X^2 against $1/V$ with best-fit straight lines through the origin.

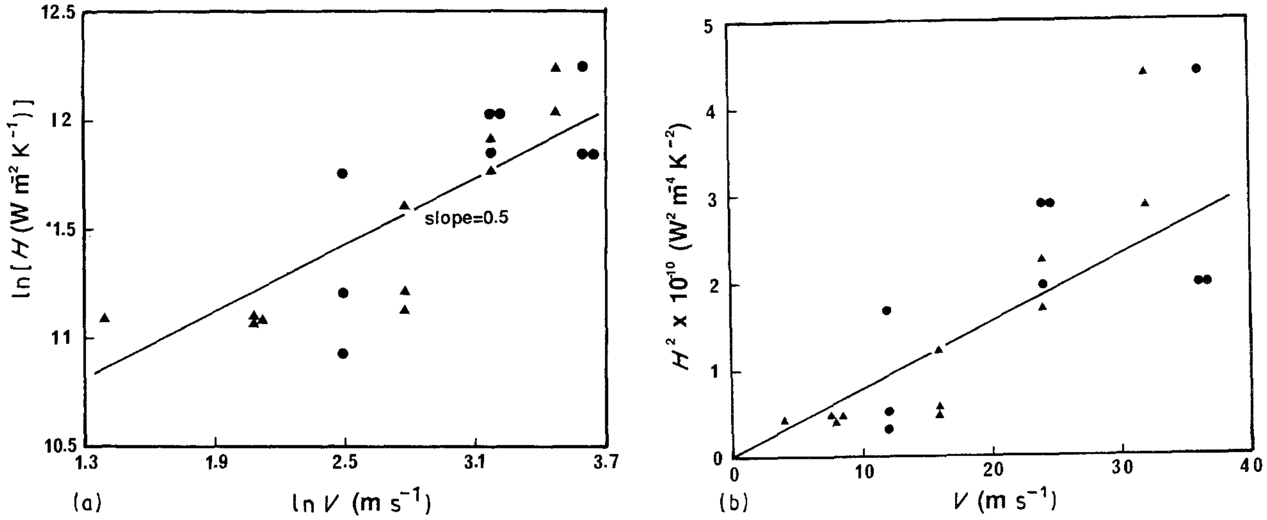

Figure 5 Variation of heat transfer coefficient H with wheel speed V in melt-spun (●) Ni–Al alloys and (▲) 316L stainless steel: (a) ln H against ln V with best-fit straight lines with a slope of 1/2; and (b) H^2 against V with best-fit straight line through the origin.

Equations 3 to 5:

$$\left(\frac{\mathrm{d}T}{\mathrm{d}t}\right)\left(\frac{Q^{1/4}}{V}\right) = a_3 \tag{6}$$

$$\left(\frac{\mathrm{d}T}{\mathrm{d}t}\right)\left(\frac{X^2}{Q^{1/4}}\right) = a_4 \tag{7}$$

where $a_3 = (a_2/a_1)^{1/2}(T_\mathrm{I} - T_\mathrm{W})/\rho C$ and $a_4 = a_1 a_3$. Figs 6a and b and 7a and b show that the measured cooling rates in Table I agree quite well with Equations 6 and 7, with good agreement between measured and predicted values of a_3 and a_4, as shown in Table III.

4.3. Solidification mechanism

On micrographs such as Fig. 2a and b, the columnar grain structure and the segregation-free region adjacent to the bottom ribbon surface indicate that melt-spun Ni–Al and 316L stainless steel ribbons solidify in the following way. Liquid in the melt puddle cools until solidification is nucleated on the bottom surface, partly because the liquid temperature is lowest adjacent to the melt-spinning wheel, and partly because the wheel surface can act as a nucleation catalyst. Nucleated grains solidify laterally until the wheel surface is completely covered, and a stable set of grains then continues to solidify in a columnar way through the ribbon thickness. Although some competitive grain growth may take place during columnar solidification, the columnar grain diameter is determined primarily by a balance between the initial rates of nucleation and lateral grain growth on the wheel surface.

At the nucleation point, the liquid is sufficiently undercooled below the equilibrium solidus temperature that the solidification velocity exceeds the absolute stability velocity [5, 20], and the initial stage of

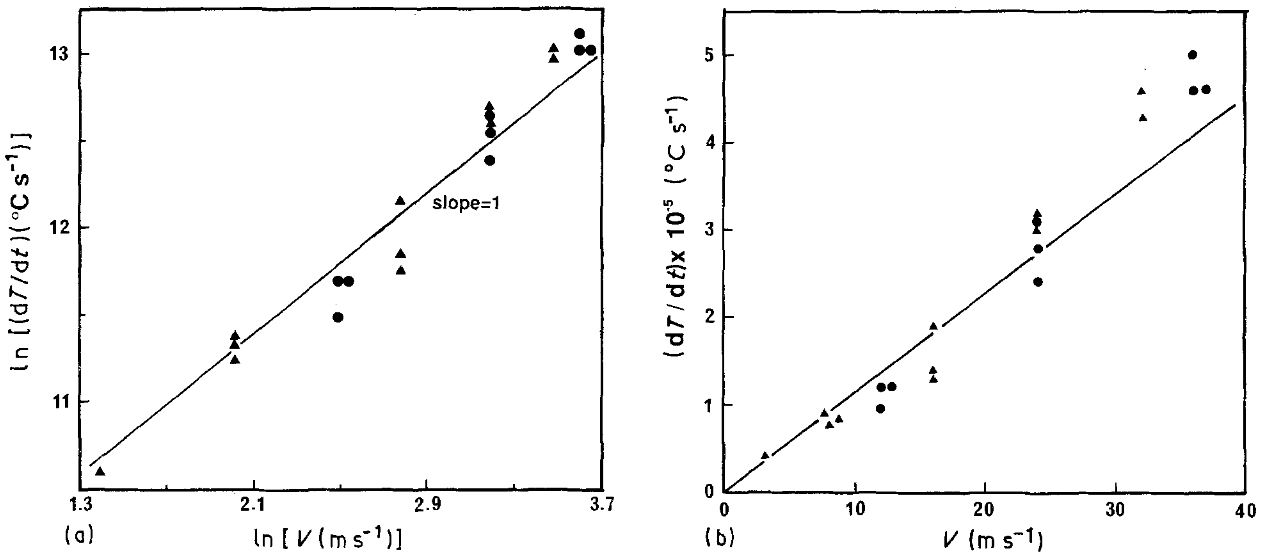

Figure 6 Variation of average cooling rate dT/dt with wheel speed V in melt-spun (●) Ni–Al alloys and (▲) 316L stainless steel: (a) ln (dT/dt) against ln V with best-fit straight line with a slope of unity; and (b) dT/dt against V with best-fit straight line through the origin.

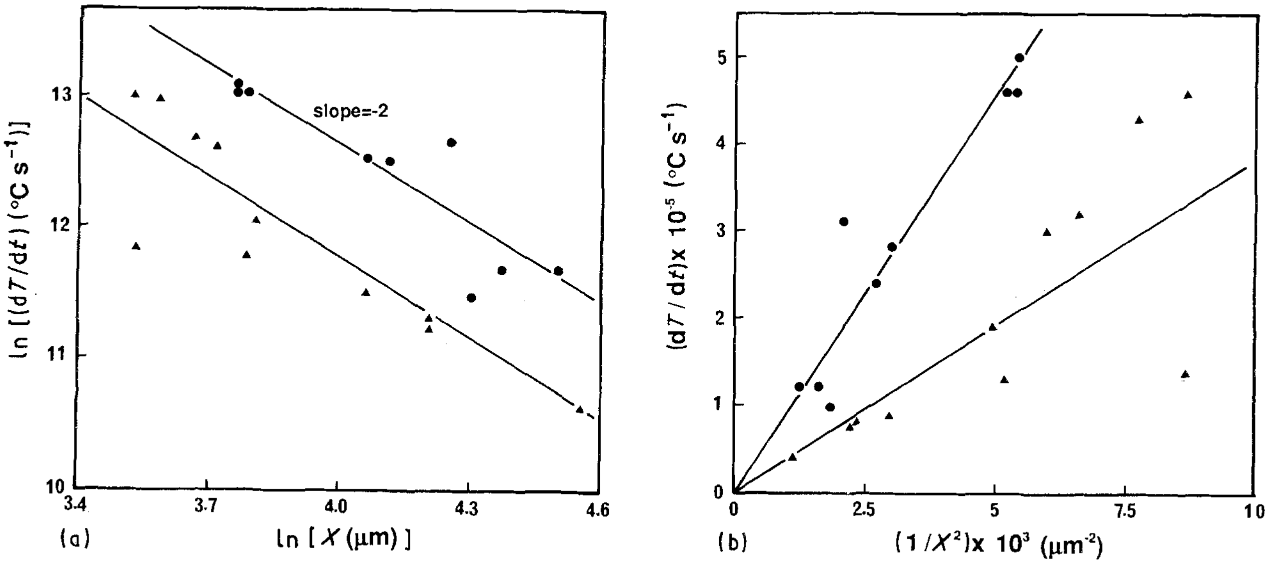

Figure 7 Variation of average cooling rate dT/dt with ribbon thickness X in melt-spun (●) Ni–Al alloys and (▲) 316L stainless steel: (a) ln (dT/dt) against ln X with best-fit straight lines with a slope of − 2; and (b) dT/dt against $1/X^2$ with best-fit straight lines through the origin.

TABLE III Measured and calculated constants in the relationships $X^2V/Q^{1/2} = a_1$, $H^2/V = a_2$, $(\mathrm{d}T/\mathrm{d}t)Q^{1/4}/V = a_3$ and $(\mathrm{d}T/\mathrm{d}t)X^2/Q^{1/4} = a_4$ (see text for details)

Constant		Alloy	
		Ni–5Al	316L
a_1 ($m^{3/2}$ sec$^{-1/2}$),	measured	4.5×10^{-5}	2.3×10^{-5}
a_2 (W^2 sec m^{-5} K^{-2}),	measured	7.8×10^8	7.8×10^8
a_3 ($Km^{1/4}$ sec$^{-1/4}$),	measured	4.8×10^2	4.4×10^2
	calculated	1.4×10^3	1.7×10^3
a_4 ($Km^{5/4}$ sec$^{1/4}$),	measured	2.2×10^{-2}	9.1×10^{-3}
	calculated ($a_1 \times a_3$ meas.)	2.2×10^{-2}	9.9×10^{-3}
	calculated ($a_1 \times \bar{a}_3$ calc.)	6.3×10^{-2}	3.9×10^{-2}

columnar solidification is partitionless with a planar solid–liquid interface. As columnar solidification proceeds, evolution of latent heat causes the solid–liquid interface temperature to increase and the solidification velocity to decrease. When the solidification velocity falls below the absolute stability velocity, the planar solid–liquid interface is destabilized and a cellular segregation pattern is developed within the columnar grains. The position of the transition from partitionless solidification to cellular segregation depends on the initial nucleation temperature in the liquid and the rate of recalescence.

4.4. Latent heat evolution

Fig. 8 shows a schematic cooling curve with a solidification arrest during melt-spinning of a pure material, assuming no thermal gradients in the ribbon, i.e. perfect Newtonian conditions during cooling and solidification. The liquid undercools to a temperature T_N below the equilibrium melting point T_M before solidification is nucleated, followed by recalescence to a steady-state growth plateau at a temperature T_G, also below the equilibrium melting point. The latent

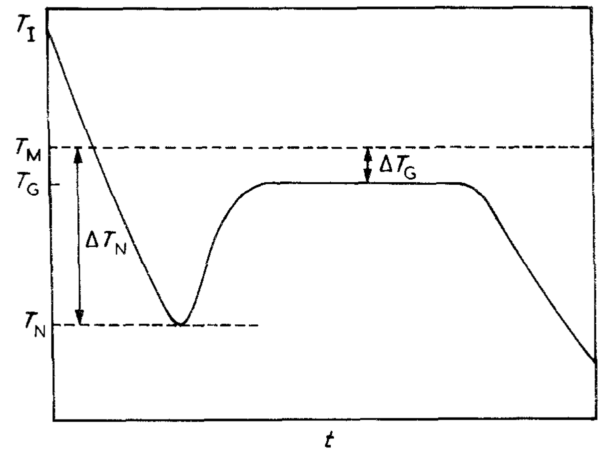

Figure 8 Schematic solidification arrest on cooling curve during melt-spinning, showing undercooling to a temperature T_N before nucleation, followed by recalescence to a steady-state growth plateau at a temperature T_G.

heat liberated by solidification is dissipated partly by heat transfer across the ribbon–wheel interface and partly by a rise in ribbon temperature [5, 6, 11]:

$$L\rho v = H(T - T_W) + X\rho C(dT/dt) \quad (8)$$

where $v = dy/dt$ is the columnar solidification rate, y is the thickness solidified, and dT/dt is now the rate of increase in ribbon temperature. Equation 8 can be integrated to describe the recalescence and steady-state growth plateau on the schematic cooling curve in Fig. 8, assuming linear solidification kinetics:

$$v = M\Delta T \quad (9)$$

where M is the solid–liquid interface mobility, and $\Delta T = T_M - T$ is the undercooling in the liquid at the solid–liquid interface.

On the steady-state growth plateau, $dT/dt = 0$, so that the second term on the right-hand side of Equation 8 can be ignored. The steady-state growth undercooling ΔT_G and solidification rate v_G on the plateau are then given by

$$\Delta T_G = H(T_M - T_W)/(H + L\rho M) \quad (10)$$

$$v_G = HM(T_M - T_W)/(H + L\rho M) \quad (11)$$

Taking typical values of $H = 10^5\,\mathrm{W\,m^{-2}\,K^{-1}}$ from Table I and $M = 0.1\,\mathrm{m\,sec^{-1}\,K^{-1}}$ [21], ΔT_G and v_G are approximately 0.5 K and 5 mm sec^{-1}, respectively.

In the recalescence region, dT/dt is large so that the first term on the right-hand side of Equation 8 can be ignored. Equation 8 can then be integrated from the nucleation temperature T_N at $y = 0$, to show that the fractional thickness solidified (y/X) increases linearly with increasing temperature during recalescence:

$$y/X = C(T - T_N)/L \quad (12)$$

Recalescence is completed and the steady-state plateau is reached when $T = T_G \simeq T_M$, so that the fraction solidified at the transition from recalescence to steady-state growth is given by $C\Delta T_N/L$, where ΔT_N is the nucleation undercooling.

When Newtonian cooling conditions are not maintained during solidification, latent heat remains concentrated in the vicinity of the solid–liquid interface. A temperature inversion builds up ahead of the solid–liquid interface, and Equations 8 to 13 underestimate the rate of recalescence. Computer calculations show that this can happen at the higher values of heat transfer coefficient [15–17]. Perfect Newtonian cooling conditions are not maintained during melt-spinning of Ni–Al and 316L stainless steel, as shown by the heat flow analysis in Fig. 3c, and by the lack of recalescence on the top surface cooling curves in Fig. 1.

4.5. Segregation

Melt-spinning of alloys can be considerably more complicated than for pure materials, because of the segregation of alloying elements during solidification. However, the solidification behaviour of low freezing-range alloys such as Ni–Al and 316L stainless steel is not too different from that described in the previous section for pure materials. Fig. 9a to c show a schematic phase diagram for a low freezing-range binary alloy, and with the corresponding molar free energy–composition curves during nucleation and steady-state growth. A melt-spun alloy of composition c_0 nucleates at a temperature T_N below the equilibrium solidus temperature T_S, forming solid nuclei with a composition between c_0 and c_N. Nucleation with a solid composition c_0 requires no diffusion, whereas nucleation with a solid composition c_N corresponds to the maximum driving force, as shown by the parallel tangent construction on Fig. 9b. The solid nuclei solidify laterally until the wheel surface is completely covered, and a stable set of grains then continues to solidify in a columnar way through the ribbon thickness. For planar-front columnar solidification, the temperature recalesces to a steady-state growth plateau at a temperature T_G below the equilibrium solidus, and the fractional thickness solidified during recalescence increases linearly with increasing temperature, as given by Equation 12.

Fig. 10 shows profiles of composition and chemical potential through the solidifying interface during steady-state growth. The only solid composition for which steady-state growth is possible is c_0, and the steady-state undercooling and solidification rate are given by Equations 10 and 11, with undercoolings now measured below the solidus temperature T_S instead of the melting point T_M. The liquid composition at the solid–liquid interface, c_L, adjusts to provide a suitable driving force for the two alloy components:

$$v_G = M_A(\mu_{AL} - \mu_{AS}) = M_B(\mu_{BL} - \mu_{BS}) \quad (13)$$

where M_A and M_B are solid–liquid interface mobilities, μ_{AL} and μ_{BL} are chemical potentials for liquid composition c_L at T_G, μ_{AS} and μ_{BS} are chemical potentials for solid composition c_0 at T_G, and solidification kinetics are again assumed to be linear. Equations 8, 9 and 13 are sufficient to fix values of v_G, ΔT_G and c_L for given conditions of heat transfer coefficient and variation of chemical potential with temperature and composition. Solute trapping [21, 22] can cause deviations

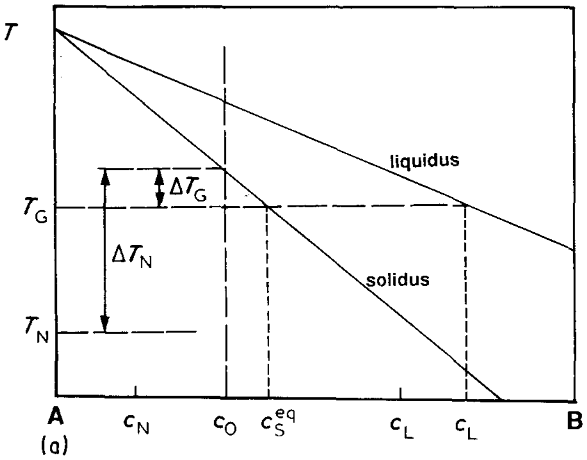

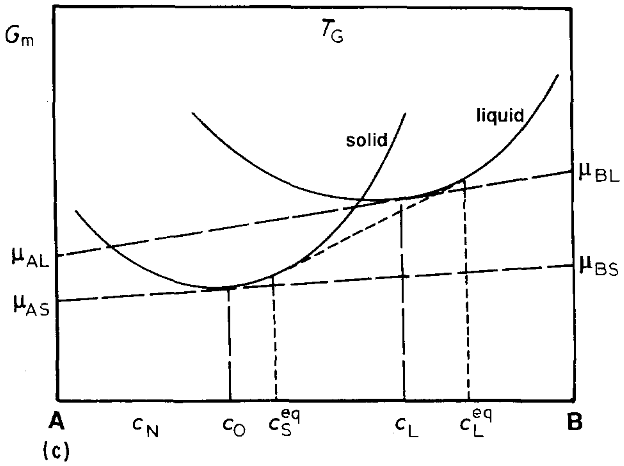

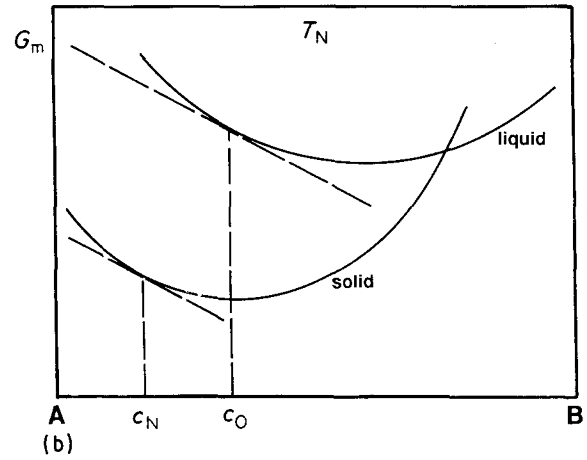

Figure 9 (a) Schematic phase diagram for a low freezing-range binary alloy. Corresponding molar free energy–composition curves at (b) the nucleation temperature T_N, and (c) the steady-state growth temperature T_G.

from Equation 13 at solidification rates greater than $\sim D/a$, where D is the liquid diffusion coefficient and a is the atomic separation. A typical value of D/a is $1\ \mathrm{m\,sec^{-1}}$ for most metals, considerably greater than v_G from Equation 11, so that solute trapping is only significant in the early stages of recalescence, and Equation 13 is valid during steady-state growth.

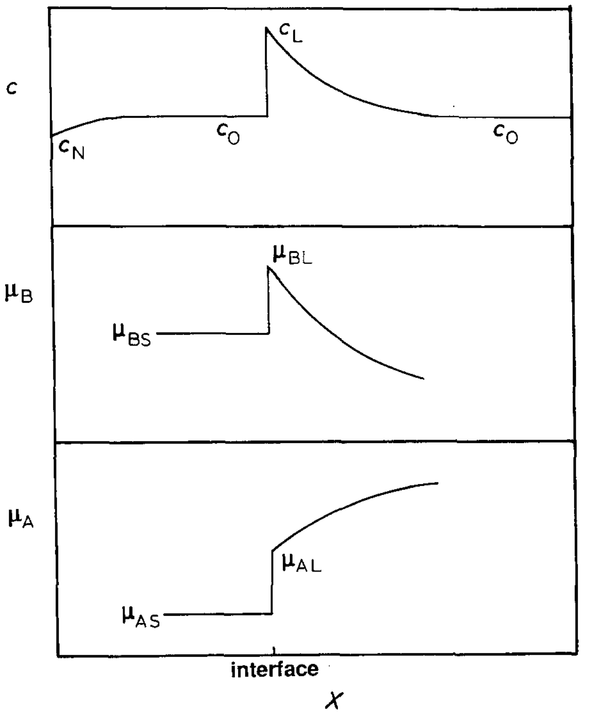

Figure 10 Composition and chemical potential profiles through the solid–liquid interface during steady-state growth.

As recalescence takes place, the temperature increases towards T_G and the solidification rate decreases towards v_G. Cellular breakdown is initiated when the solidification rate falls below the absolute stability velocity v_A, which corresponds to an undercooling ΔT_A:

$$v_A = mDc_0L\rho(1 - k_0)/k_0^2 T_S \sigma \qquad (14)$$

$$\Delta T_A = v_A/M \qquad (15)$$

where m is the liquidus slope, k_0 is the equilibrium partition coefficient and σ is the solid–liquid interfacial energy [20]. From Equation 12, the fractional segregation-free thickness is $C(T_A - T_N)/L$. When melt-spun microstructures such as Fig. 2a and b show a transition from partitionless to cellular solidification, measurements of the fractional segregation-free thickness can be used together with Equations 12, 14 and 15 to estimate the nucleation temperature.

Relative variations in nucleation temperature can be determined in this way, but absolute values are inaccurate, because Newtonian conditions are not maintained during recalescence. As shown in Fig. 2a and b, the segregation-free thickness varies along the length of melt-spun Ni–Al and 316Al stainless steel ribbons, indicating a variation in the nucleation temperature from place to place on the melt-spinning wheel surface. Table II includes some maximum nucleation undercoolings in melt-spun Ni–Al alloys and 316L stainless steel, calculated from the measured fractional segregation-free thickness using Equations 12, 14 and 15. Fig. 11 shows the maximum nucleation undercooling plotted as a function of measured cooling rate, and indicates that the nucleation undercooling is approximately proportional to the cooling rate in melt-spun Ni–Al alloys and 316L stainless steel.

4.6. Grain size

The mean area of the wheel surface covered by each grain during nucleation and lateral growth can be

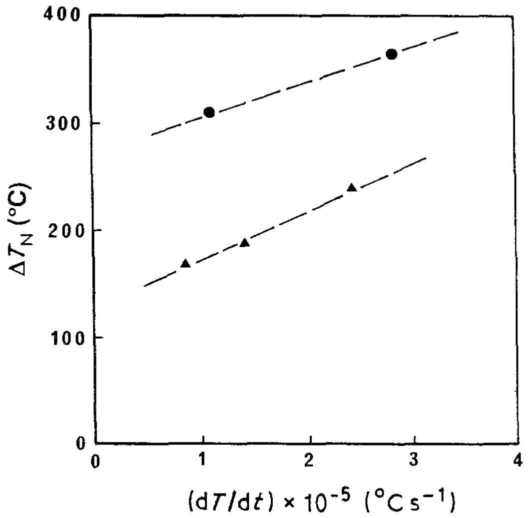

Figure 11 Maximum nucleation undercooling in the liquid before the onset of solidification, measured from the maximum segregation-free thickness, as a function of measured cooling rate in melt-spun (●) Ni–Al alloys and (▲) 316L stainless steel. Best-fit linear variations shown by dashed lines.

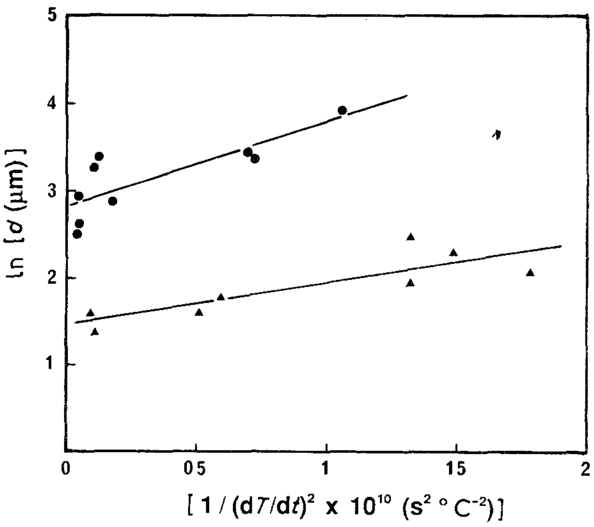

Figure 12 Columnar grain size, measured parallel to the long ribbon dimension and close to the wheel surface, as a function of measured cooling rate in melt-spun (●) Ni–Al alloys and (▲) 316L stainless steel. Best-fit linear variations shown by dashed lines.

expressed independently in terms of the average lateral grain diameter d, the average lateral solidification rate at the average nucleation temperature v_N, and the average nucleation rate per unit area of wheel surface N:

$$\pi\left(\frac{d}{2}\right)^2 = \pi\left(\frac{v_N t_S}{2}\right)^2 = \frac{1}{N t_S} \qquad (16)$$

Eliminating the local solidification time t_S:

$$d^3 = 4v_N/\pi N \qquad (17)$$

The solidification velocity and nucleation rate both depend upon the nucleation temperature. For solid nuclei of composition c_0 growing with linear solidification kinetics, the solidification velocity is given by Equation 9, with undercooling now measured below the T_0 temperature at which solid and liquid of composition C_0 are in equilibrium:

$$v_N = M\Delta T_N \qquad (18)$$

The nucleation rate is given by [23, 24]

$$\begin{aligned} N &= \frac{nkT_N}{h}\exp\left(\frac{-Q}{kT_N}\right)\exp\left(\frac{-16\pi\sigma^3 T_0^2 f(\theta)}{3L^2\rho^2\Delta T_N^2 kT_N}\right) \\ &= N_0\exp\left(\frac{-Q'}{\Delta T_N^2}\right) \qquad (19) \end{aligned}$$

where n is the number of available nucleation sites per unit area of wheel, k is Boltzmann's constant, h is Planck's constant, Q is the activation energy for addition of an atom to a critical nucleus, $f(\theta) = (2 - 3\cos\theta + \cos^3\theta)/4$, θ is the contact angle for a solid nucleus on the wheel surface, and N_0 and Q' are approximately constant with temperature. Combining Equations 17 to 19 gives the grain size as a function of nucleation undercooling:

$$\ln d = \ln\left(\frac{4M}{\pi N_0}\right) + \ln\Delta T_N + \left(\frac{Q'}{\Delta T_N^2}\right) \qquad (20)$$

The third term on the right-hand side of Equation 20 is much more sensitive to nucleation undercooling than the second term, so that $\ln d$ is expected to increase inversely with the square of the nucleation undercooling.

Fig. 12 shows ln (grain size) plotted as a function of the inverse square of the cooling rate, from the measurements in Table II for melt-spun Ni–Al alloys and 316L stainless steel. The variation of grain size with cooling rate can be expressed approximately as

$$\ln d \propto \frac{1}{(dT/dt)^2} \qquad (21)$$

Comparing Equations 20 and 21, the measurements of grain size in melt-spun Ni–Al alloys and 316L stainless steel again indicate that the nucleation undercooling is proportional to the cooling rate, in agreement with the segregation measurements shown in Fig. 11.

5. Conclusions

Photocalorimetric measurements of top surface temperatures during melt-spinning of Ni–Al and 316L stainless steel ribbons show that cooling conditions are near-Newtonian, with mean cooling rates, heat transfer coefficients and Nusselt numbers in the range 4×10^4 to 5×10^5 K sec^{-1}, 5×10^4 to 3×10^5 W m^{-2} K^{-1} and 0.07 to 0.22, respectively, for wheel speeds in the range 4 to 36 m sec^{-1}. The mean cooling rate during melt-spinning is directly proportional to the wheel speed and inversely proportional to the square of the ribbon thickness.

Melt-spun Ni–Al and 316L stainless steel ribbons exhibit a columnar solidification microstructure through the ribbon thickness, and a segregation-free region adjacent to the wheel surface. Solidification takes place by heterogeneous nucleation of the undercooled liquid on the wheel surface to form a stable set of columnar grains, followed by partitionless solidification during recalescence in the initial stages of columnar through-thickness growth, and finally cellular breakdown and segregated solidification in the later stages of columnar through-thickness growth. The columnar grain size decreases and the fractional segregation-free thickness increases with increasing wheel speed and cooling rate. The variations of grain size and segregation-free thickness with cooling rate indicate that the nucleation undercooling in the liquid is proportional to the cooling rate.

Acknowledgements

We would like to thank Professor Sir Peter Hirsch for provision of laboratory facilities, and the UK Science and Engineering Council and the Korean Science and Engineering Foundation for financial support of this research programme.

References

1. B. CANTOR (ed.), "Rapidly Quenched Metals III" (Metals Society, London, 1978).
2. T. MASUMOTO and K. SUZUKI (eds), "Rapidly Quenched Metals IV" (Japan Institute of Metals, Sendai, 1982).
3. S. STEEB and H. WARLIMONT (eds), "Rapidly Quenched Metals V" (North-Holland, Amsterdam, 1985).
4. R. W. COCHRANE and J. O. STROM-OLSEN (eds), "Rapidly Quenched Metals 6" (Elsevier, London, 1988).
5. B. CANTOR, in "Science and Technology of the Undercooled Melt", edited by P. R. Sahm, H. Jones and C. M. Adam (Nijhoff, Dordrecht, 1986) p. 3.
6. *Idem*, in "Rapidly Solidified Amorphous and Crystalline Alloys", edited by B. H. Kear and B. C. Giessen (Elsevier North-Holland, New York, 1982) p. 317.
7. H. JONES, *Rep. Prog. Phys.* **36** (1973) 1425.
8. *Idem*, "Rapid Solidification of Metals and Alloys" (Institution of Metallurgists, London, 1982).
9. M. HANSEN and K. ANDERKO, "The Constitution of Binary Alloys" (McGraw-Hill, New York, 1958).
10. B. P. BEWLAY and B. CANTOR, *Int. J. Rapid Solidifn* **2** (1986) 107.
11. C. HAYZELDEN, J. J. RAYMENT and B. CANTOR, *Acta Metall.* **31** (1983) 379.
12. A. G. GILLEN and B. CANTOR, *ibid.* **33** (1985) 1813.
13. A. J. B. VINCENT, B. P. BEWLAY, B. CANTOR, R. J. ZABALA, R. P. LaFORCE, S. C. HUANG and L. A. JOHNSON, *J. Mater. Sci. Lett.* **6** (1987) 121.
14. H. S. CARSLAW and J. C. JAEGER, "Conduction of Heat in Solids" (Oxford University Press, Oxford, 1959).
15. C. HAYZELDEN, DPhil thesis, University of Sussex (1984).
16. T. W. CLYNE, *Metall. Trans.* **15B** (1984) 369.
17. R. C. RUHL, *Mater. Sci. Eng.* **1** (1967) 313.
18. J. H. VINCENT, J. G. HERBERTSON and H. A. DAVIES, in T. Masumoto and K. Suzuki (eds), "Rapidly Quenched Metals IV", Vol. 1 (Japan Institute of Metals, Sendai, 1982) p. 77.
19. A. G. GILLEN, T. C. WILLIS and B. CANTOR, to be published.
20. W. J. BOETTINGER, D. SCHECHTMAN, R. J. SCHAEFFER and F. S. BIANCELLO, *Metall. Trans.* **15A** (1984) 55.
21. M. HILLERT and B. SUNDMAN, *Acta Metall.* **24** (1976) 731.
22. J. C. BAKER and J. W. CAHN, *ibid.* **17** (1969) 575.
23. D. TURNBULL, *J. Appl. Phys.* **21** (1950) 1022.
24. B. CANTOR and R. D. DOHERTY, *Acta Metall.* **27** (1979) 33.

Received 25 January
and accepted 26 February 1990